ARTICLES
https://doi.org/10.1038/s41551-019-0455-7
nature biomedical engineering

A nanoelectrode array for obtaining intracellular recordings from thousands of connected neurons

Jeffrey Abbott[1,2,3], Tianyang Ye[1], Keith Krenek[1], Rona S. Gertner[2], Steven Ban[2], Youbin Kim[3], Ling Qin[1], Wenxuan Wu[1], Hongkun Park[2,3]* and Donhee Ham[1]*

Current electrophysiological or optical techniques cannot reliably perform simultaneous intracellular recordings from more than a few tens of neurons. Here we report a nanoelectrode array that can simultaneously obtain intracellular recordings from thousands of connected mammalian neurons in vitro. The array consists of 4,096 platinum-black electrodes with nanoscale roughness fabricated on top of a silicon chip that monolithically integrates 4,096 microscale amplifiers, configurable into pseudocurrent-clamp mode (for concurrent current injection and voltage recording) or into pseudovoltage-clamp mode (for concurrent voltage application and current recording). We used the array in pseudovoltage-clamp mode to measure the effects of drugs on ion-channel currents. In pseudocurrent-clamp mode, the array intracellularly recorded action potentials and postsynaptic potentials from thousands of neurons. In addition, we mapped over 300 excitatory and inhibitory synaptic connections from more than 1,700 neurons that were intracellularly recorded for 19 min. This high-throughput intracellular-recording technology could benefit functional connectome mapping, electrophysiological screening and other functional interrogations of neuronal networks.

The patch-clamp electrode is valued for its high-sensitivity intracellular recording that can measure not only propagation of action potentials (APs) in neurons but also subthreshold events such as postsynaptic potentials (PSPs). Dense, parallel execution of such high-sensitivity intracellular recording across a neuronal network is a key technological pursuit in neurobiology[1–4], but has never been achieved[5]. The patch-clamp electrode itself is not well suited for scaling into a dense array, and only about 10 parallel patch recordings of neurons have been made to date[6]. Top-down fabricated nanoelectrode arrays have been developed with the aim of parallelizing intracellular recording[7,8], but these intracellular interfaces exhibited fidelities far inferior to the patch clamp and could not be applied to neuronal networks.

Here we report a neuroelectronic interface that is capable of massively parallel intracellular neuronal recording. It consists of 4,096 recording and stimulation sites, or 'pixels,' of platinum-black (PtB) electrodes, defined on top of a complementary metal-oxide-semiconductor (CMOS) chip––that is, a silicon integrated circuit (IC)––that monolithically integrates 4,096 microscale amplifiers. The combination of the nanoscale-rough surface morphology of the PtB electrode and the on-site amplification, configurable between a pseudocurrent-clamp (pCC) and a pseudovoltage-clamp (pVC) mode with a continued electrode current injection, enables stable, sensitive intracellular recording of subthreshold membrane potentials (in pCC mode), ion-channel currents (in pVC mode) and concurrent stimulation of neurons at each pixel. Arrayed operation in pCC mode can record both APs and PSPs from thousands of connected mammalian neurons cultured in vitro. This merging of parallelism for network coverage and intracellular recording with subthreshold sensitivity enables an explicit network-wide mapping of over 300 excitatory and inhibitory synaptic connections from more than 1,700 neurons intracellularly recorded for only 19 min. This level of experimental throughput can transform a broad range of functional interrogations of neuronal networks, such as functional connectome mapping and high-throughput electrophysiological screening.

The capabilities of this CMOS neuroelectronic interface (CNEI) can be highlighted in comparison to three other mainstream electrophysiology techniques. First, CMOS microelectrode arrays (MEAs)[9–13] featuring as many as 65,000 electrodes or circuit channels[12], can monitor a large number of neurons, but they are an extracellular technique and so cannot measure subthreshold events that are critical for examining the synaptic connectivity of neurons[5]. By contrast, our CNEI subsumes the capability of the CMOS MEA (extracellular measurements of a large number of cells) and expands that parallelism to intracellular measurements. Second, the microfluidic planar patch-clamp array[14–16] is an electrophysiological drug-screening tool that can perform parallel intracellular recording, but only from disconnected, non-neuronal cells due to its construction. By contrast, our CNEI can measure connected neurons (including induced pluripotent stem cell (iPSC)-derived neurons) that form a network and can provide both an ion-channel assay (in the pVC mode) and a synaptic-connection assay (in the pCC mode), directly measuring the effects of drugs on ion-channel currents and network connectivity and dynamics. Third, optical electrophysiology, based on voltage-sensitive dyes or proteins and Ca^{2+} indicators, features high signal-to-noise ratios, and when coupled with optical stimulation techniques, provides a promising path towards network-wide recording and stimulation[17,18]. To date, however, network-scale monitoring has been performed mostly with indirect Ca^{2+} imaging[19–22], with membrane potential recordings being limited to tens of neurons[17,18,23–25].

The remainder of this Article provides a detailed account of the development of the CNEI and the key experiments that highlight its performance.

The CMOS neuroelectronic interface

CMOS electronics––that is, silicon ICs that form the heart of today's computers––are known for the scalability that can integrate a

[1]John A. Paulson School of Engineering and Applied Sciences, Harvard University, Cambridge, MA, USA. [2]Department of Chemistry and Chemical Biology, Harvard University, Cambridge, MA, USA. [3]Department of Physics, Harvard University, Cambridge, MA, USA. *e-mail: Hongkun_Park@harvard.edu; donhee@seas.harvard.edu

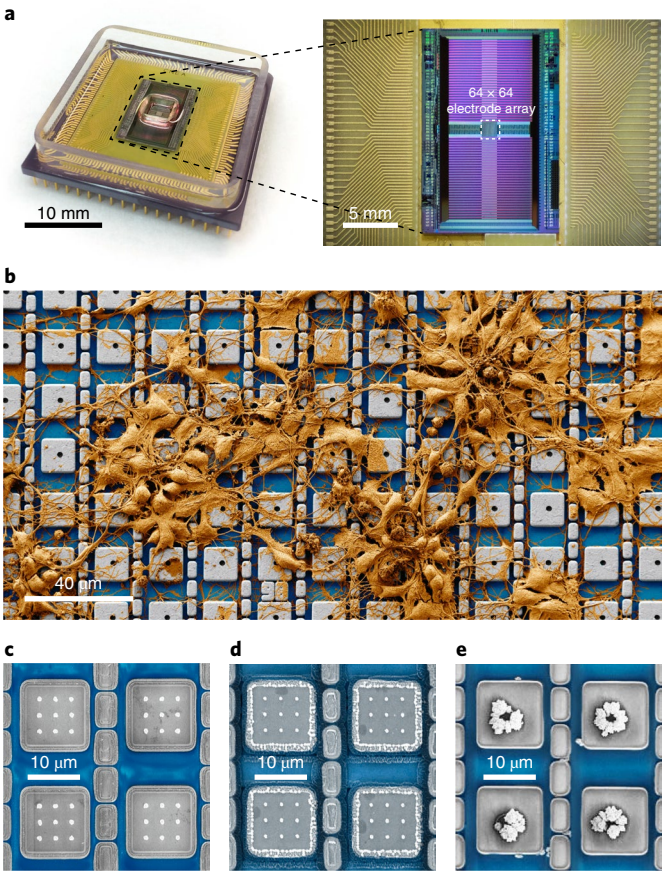

Fig. 1 | The CNEI. a, A CMOS-activated PtB electrode array packaged with a microfluidic well (left) in which neurons are cultured. Its CMOS IC (right) contains an array of 64 × 64 pixel pads (20 μm pitch) at its centre. On each pad PtB-coated Pt electrodes are built. **b**, False coloured scanning electron microscope image of neurons cultured on top of the electrode array of an example CNEI device. Actual recording experiments are performed with much higher neuron densities containing three to six cell layers covering the entire electrode array (Supplementary Fig. 4). **c**–**e**, Scanning electron microscope images (top view) of the three different structures of Pt electrodes after PtB deposition, all of which have been demonstrated for intracellular access: PtB-coated vertical Pt nanoneedles (**c**; dimensions before PtB coating: 9 Pt vertical nanoneedles per pad at a 3 μm pitch, about 100 nm diameter, 1 μm height); PtB-coated vertical Pt nanoneedles with PtB-coated Pt pad edge electrodes (**d**; dimensions of the Pt pad edge electrode before PtB coating: approximately 10 μm long ridge along each pad edge, up to 1 μm height); and PtB-coated Pt planar hole electrodes (**e**; each Pt hole has a 2 μm diameter opening and is 1.2 μm deep, as PtB is electrodeposited into the hole, a micrometre-scale mound of PtB builds). Since the electrode structure in **d** proved to be the most effective for highly parallel intracellular recording, the majority of the data presented in the manuscript and Supplementary Figures are with this electrode structure. The hole structure of **e** is fabricated with a much-simplified process in comparison to the vertical nanoneedles and thus could be an attractive alternative in the future, once further optimized.

massive number of transistors into a chip-scale footprint. The core of our CNEI is one such CMOS IC, which we designed (Fig. 1a, right). At the centre of the IC is an array of 64 × 64 = 4,096 surface aluminium (Al) pads, each 10.5 μm × 10.5 μm and with a pitch of 20 μm (Fig. 1b). On each pad, PtB-coated platinum (Pt) electrodes––another critical component of our neuroelectronic interface––are built. Each pad, which defines a unit recording–stimulation site, or a pixel, is wired to its own active circuit located outside the centre pad-array area (Supplementary Fig. 3a). We chose the pixel pad pitch of 20 μm to enable each pixel to couple to one in vitro rat cortical neuron (soma diameter approximately 20 μm). The heart of each pixel's active circuit is a low-noise voltage amplifier and a current injector: this active circuit block can be arranged into either pCC or pVC configuration (Supplementary Fig. 3b; see also Fig. 2b,c). We use the prefix 'pseudo' because our current- and voltage-clamp configurations end up fixing the current and the voltage of the electrode rather than those of the neuron due to the particular nature of our electrode–neuron interface, as discussed below. On each pad, we post-fabricate Pt electrodes of varying geometries, such as vertical nanoneedles, vertical nanoneedles with pad edge lines, and hole electrodes, using standard top-down technology (Supplementary Fig. 1a–d and Methods). We then package the CMOS IC with a microfluidic well into a chip carrier (Fig. 1a, left and Supplementary Fig. 1e) and place it on a custom-designed printed circuit board (Supplementary Fig. 1f). The final step of the CNEI construction is the deposition of PtB on the Pt electrodes by electrodeposition[26] (Fig. 1c–e and Supplementary Fig. 2a).

The CNEI differs from our earlier CMOS-nanoelectrode array[8], which could intracellularly record hundreds of cardiomyocytes but was not applicable to even a small number of neurons. We engineered the pixel's passive electrodes and active circuit to enable stable and controlled intracellular recordings with sufficient sensitivity to measure subthreshold PSPs (pCC mode) and ion-channel currents (pVC mode) of mammalian neurons. This had previously only been possible with patch-clamp electrodes.

One advantage of this design is that the PtB coating that adds nanometre-scale roughness to the Pt electrode (Fig. 1c–e) increases its surface area and lowers its impedance (Z_e in Fig. 2a) by more than ten times (the measured electrode impedance per pixel is around 300 kΩ at 5 kHz (around 95 pF): Supplementary Fig. 2b and Methods). The reduced electrode impedance enhances the cell-to-amplifier signal transfer, and thus the recording sensitivity. This reduced electrode impedance also lowers the likelihood of large (micrometre-scale) gas bubble generation during the electrode current injection that is used to permeabilize the neuron's cell membrane for intracellular access in both pCC and pVC configurations. This prevention of large bubble formation is critical because those bubbles could disrupt the membrane–electrode interface and possibly damage the neuron. For example, Pt vertical nanoneedles were able to gain intracellular access to neurons with current injection only when coated with PtB (Fig. 1c and Supplementary Fig. 5). Another advantage of the PtB nanoscale roughness, beside the reduced impedance, is its physical role in helping to form a tight and stable seal with the cell membrane[27–30]. For example, when the planar Pt hole is electrodeposited with PtB, a micrometre-scale mound of PtB with nanometre-scale surface roughness forms (Fig. 1e). While the overall structure is not as sharply protruding as the PtB-coated vertical nanoneedle (Fig. 1c,d), it is still capable of intracellular access (Supplementary Fig. 5). This suggests that the nanoscale surface roughness of PtB itself may help establish a stable seal. Supplementary Table 1 and Supplementary Discussion 1 present details of our investigation of intracellular access using the various PtB-coated electrode structures shown in Fig. 1c–e. The majority of the data presented in the remainder of this Article and the Supplementary Information (all data except Fig. 2f,g, Supplementary Figs. 5 and 13) are from the PtB-coated vertical nanoneedles with PtB-coated pad edge electrodes (Fig. 1d); the edge electrodes provide an additional current flow path, further reducing the probability of large gas bubbling, thus leading to intracellular coupling with the highest yield.

A second advantage is the configurability of the active pixel circuit between the pCC and pVC modes. For membrane potential measurement, the pixel circuit is arranged into the pCC configuration, consisting of a current injector that runs in parallel with a

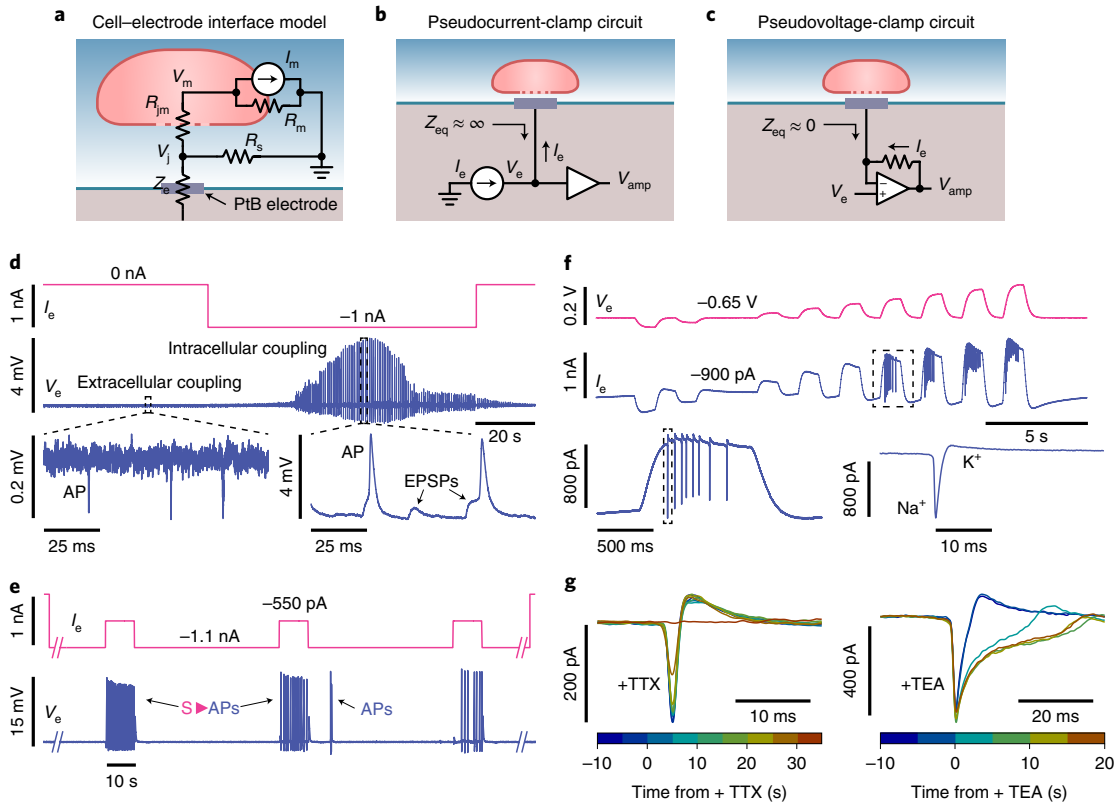

Fig. 2 | Intracellular recording and stimulation of disassociated rat neurons using the pCC and pVC configurations. a, A simplified small-signal model of the electrode–neuron interface is shown, including the membrane potential V_m, membrane current I_m, junctional membrane resistance R_{jm}, seal resistance R_s, and membrane resistance R_m. **b**,**c**, Each pixel circuit can be arranged into either pCC or pVC configuration. The pCC configuration consists of a current injector with output current I_e, and a high input impedance (Z_{eq}) voltage amplifier ($A_v \approx 30$ V/V) that operate in parallel; the pVC configuration is a low-input impedance transimpedance amplifier ($R_f \approx 750$ MΩ). **d**, Extracellular measurement of a neuron transitions to intracellular measurement with $I_e = -1$ nA applied through the pixel in the pCC configuration, resulting in around 20-fold improvement in AP signal amplitude. EPSPs and their triggering of an AP are also clearly visible. **e**, After attaining intracellular access in the pCC configuration, an effective positive stimulation current can be applied by adjusting I_e to a less negative value: +550 pA injections of 10 s are applied every 60 s (top), which excites the neuron to fire APs during the stimulation windows (bottom, S▶APs). **f**, Intracellular access is gained in the pVC configuration by setting V_e to −0.65 V to pass $I_e \approx -900$ pA. No spontaneous activity is observed during this process due to the low-input impedance of the pVC circuit. Voltage stimulations are used to activate the neuron's ion-channels with characteristic negative Na^+ spikes and positive K^+ repolarization currents observed. **g**, Application of the ion-channel drugs tetrodotoxin (TTX, Na^+ channel blocker, left) and tetraethylammonium (TEA, K^+ channel blocker, right) confirm the origin of the measured Na^+ and K^+ currents and highlight the pVC's capability for ion-channel drug screening applications.

high-impedance voltage amplifier (Fig. 2b; see also Supplementary Fig. 3b,g,h). This configuration permits concurrent current (I_e) injection and voltage (V_e) amplification through the same electrode. Here the voltage amplifier is designed in a bandpass-filter topology with a bandwidth from approximately 0.5 Hz to 9.4 kHz (Supplementary Fig. 3c,d) to cover the spectral ranges of APs, PSPs, and membrane potential oscillations of neurons[5].

For ion-channel current measurement, the pixel circuit is arranged into the pVC configuration, in which the current injector is turned off and the high-impedance voltage amplifier is turned into a low-impedance transimpedance amplifier with the feedback impedance R_f (approximately 750 MΩ) switched on (Fig. 2c). This pVC configuration permits concurrent voltage (V_e) application and current (I_e) recording through the same electrode.

Another advantage is the tenfold enhancement in the sensitivity of the active pixel circuits. The voltage amplifier in the pCC configuration achieves around 20 μV root mean squared (r.m.s.) measured input referred voltage noise at the electrode voltage (V_e) node (which is the amplifier input node) when integrated across 1 Hz to 4.7 kHz (Supplementary Fig. 3e,f and Methods). This noise is ten times lower than our previous design[8] and is achieved by the separation of the passive pixel pad array region and the active pixel circuit array region (Supplementary Fig. 3a). With this separation, despite the dense pixel pad pitch (20 μm), each pixel circuit can occupy a larger area (100 μm × 250 μm), so that larger transistors with lower noise can be accommodated. The transimpedance amplifier in the pVC configuration benefits from the same lower transistor noise: it achieves around 1 pA r.m.s. measured input referred current noise in the electrode current (I_e) path, when integrated across 1 Hz to 4.7 kHz (Supplementary Fig. 3n).

Fourth, both pCC and pVC configurations enable the injection of Faradaic current (I_e) through the electrode (Fig. 2b,c), which has a critical role for intracellular access in our work. The pCC configuration (Fig. 2b) has an explicit current injector that directly controls the electrode current I_e. The pVC configuration (Fig. 2c) indirectly sets the electrode current I_e by applying the electrode voltage V_e. The pVC configuration records this injected current I_e and any modulation of it due to ion-channel currents. This electrode current injection in both the pCC and pVC configurations is used to permeabilize the cell membrane and thus to create an intracellular access to neurons, either by electroporation, through nanoscale bubbles generated from hydrolysis (not to be confused with the

detrimental microscale bubbling), or by gating of the ion channels in the membrane[31] (Supplementary Discussion 2). We continue the Faradaic current injection even after the attainment of the intracellular access to maintain the membrane permeabilization, and also, critically, to compensate for leakage current from inside the neuron (and further, to manipulate the membrane potential for neuronal stimulation). Throughout this current injection, the pCC mode records the membrane potential (smaller than the real value due to signal attenuation; see below) and the pVC mode records the current injection itself and any modulation of the current injection due to membrane currents (also smaller than the real value). In this way, the pixel can perform stable, sensitive and controlled intracellular probing of subthreshold membrane potentials as well as ion-channel currents. These pCC and pVC configurations with the electrode current injection differentiate the device from our previous CMOS-nanoelectrode array[8], whose pixels combined a voltage stimulator for membrane permeabilization and a voltage amplifier for recording: those two building blocks could not run simultaneously as both deal with voltage, and the pixel was therefore unsuccessful in the intracellular recording of neurons.

Intracellular recording and stimulation of neurons

Figure 2 presents single-pixel recording and stimulation experiments with dissociated primary rat cortical neurons (cultured in vitro at high densities to form multiple cell layers; Supplementary Fig. 4). Every recorded voltage and current shown here and throughout this Article are the electrode voltage (amplifier input voltage) V_e and the electrode current I_e (Fig. 2b,c), which we measure directly.

At $I_e = 0$ A in the pCC configuration and by setting V_e at a suitable DC value to cause no bias current into the electrode in the pVC configuration (Supplementary Fig. 6a), no membrane permeabilization occurs. In this non-intracellular mode, we measure extracellular signals with AP voltage amplitudes of $\Delta V_e = 50\sim300\,\mu$V, similar to traditional MEAs[5] and current variations of $\Delta I_e = 50\sim100$ pA (Supplementary Fig. 6a). Our propensity to measure negative polarity extracellular voltage spikes 98% of the time (Supplementary Fig. 7a) indicates a tendency of the PtB electrodes to interface strongly with the neuron's soma or axon (negative spikes) over the neuron's dendrites (positive spikes)[32–34].

For intracellular modes, we pass a Faradaic current ($I_e \neq 0$ A) to induce membrane permeabilization. In the pCC mode that records V_e (Fig. 2a,b), the membrane potential V_m causes a change in V_e from its bias value (this voltage bias is set by the injected I_e), where the change in V_e is an attenuated version of V_m. Concretely, $\Delta V_e = \alpha \times \Delta V_m$, where $\alpha = R_s/(R_{jm} + R_s)$ is the pCC attenuation factor and R_s and R_{jm} are the seal and junctional membrane resistance, respectively (Fig. 2a). The electrode impedance Z_e does not appear here because the PtB coating has made Z_e small enough to render the extra attenuation due to Z_e negligible. In the pVC mode that records I_e (Fig. 2a,c), the membrane current (for example, ion-channel currents) I_m causes a change in I_e from its bias value (this current bias is set by the applied voltage V_e and is what is injected into the electrode), where the change in I_e is an attenuated version of I_m. Concretely, $\Delta I_e = \gamma \times \Delta I_m$, where $\gamma = R_m/(R_{jm} + R_m)$ is the pVC attenuation factor and R_m is the membrane resistance (see Supplementary Discussion 2 for detailed discussions of these coupling parameters).

We first examine V_e recording in the pCC configuration (Fig. 2d). At $I_e = 0$ A (no electrode current injection), no membrane permeabilization is caused and R_{jm} is much larger than R_s, to put the attenuation factor α on the order of $10^{-4}\sim10^{-3}$: this is the extracellular recording discussed earlier. To transition to intracellular access, we change I_e to a negative value in the range of −0.5 nA to −3.0 nA (for the determination of these current values, see Supplementary Fig. 5). This current induces a gradual permeabilization of the cellular membrane and causes the cell–electrode coupling to change from extracellular to intracellular (over a time course of around 10 s to a few minutes). During this transition to intracellular coupling, R_{jm} is drastically reduced, greatly increasing α and thus the amplitude of recorded APs (Fig. 2d). Concretely, α is increased to the order of $10^{-2}\sim10^{-1}$ from its extracellular value of $10^{-4}\sim10^{-3}$. While this α is still smaller than the α of the patch clamp, which is close to 1 (that is, R_{jm} is still substantially larger than R_s in this case), it is large enough to enable clear measurements of subthreshold signals such as excitatory PSPs (EPSPs) (Fig. 2d) and inhibitory PSPs (IPSPs) (Supplementary Fig. 7b) well above the noise level. Similar intracellular access with subthreshold PSP sensitivity was also achieved using iPSC-derived glutamatergic neurons (Supplementary Fig. 7c), which may provide a better model system for drug screening for human neurological diseases and/or personalized medicine.

Notably, the injection of the negative I_e is sustained throughout the pCC intracellular recording (Fig. 2d) and contrasts with other substrate-based electrode work that uses electroporation[7,8,13,27,28,35,36]. In previous substrate-based work, electroporation was performed using a voltage application and signals were recorded using a voltage amplifier, and thus electroporation and recording could not be concurrent. The purpose of our continued current injection is twofold. First, it serves to maintain the membrane permeabilization it initiated. Second, a portion (1~10 %) of the I_e enters the neuron through R_{jm} to compensate for the leakage from within the cell: such leakage is an important side effect of membrane permeabilization required for intracellular access (the remainder of I_e that does not enter the neuron through R_{jm} flows through R_s). Essentially, after the membrane has become permeabilized, the current injection has a similar role to the holding current during patch-clamp measurements, keeping the neuron's membrane potential at a value near the normal resting potential. Without this compensation, the neuronal membrane potential can be depolarized to an unhealthy value (as in the case of previous intracellular nanoelectrode works[7,8,27–30,35–41]), affecting or even preventing normal electrophysiological function. In Fig. 2d, we observe that the neuron-firing pattern does not change with intracellular access (Supplementary Fig. 8, bottom), indicating successful leakage compensation via current injection.

This intracellular recording with the sustained current injection eventually stops on its own (Fig. 2d and Supplementary Fig. 10). This is either due to the gradually decreasing R_{jm} with the I_e injection (Supplementary Fig. 11), which makes the leakage compensation imperfect, eventually hyperpolarizing the neuron and stopping its activity, or possibly because of the loss of the seal, which eventually decreases the recorded amplitude (Supplementary Discussion 2). While the intracellular recording shown in Fig. 2d lasts for about 1 min, this example is on the shorter end: in the array-wide measurements discussed below, the intracellular coupling lasts for a median duration of 8 min (Supplementary Fig. 10 is an example of longer intracellular recording).

The ability to compensate for the current leakage can be further exploited to enable direct modulation of V_m for neuronal stimulation in the pCC configuration (Fig. 2e): V_m is related to I_e by $V_m \propto \beta \times I_e$ where $\beta = R_s \times R_m/(R_{jm} + R_m)$ (see Supplementary Discussion 2). By changing I_e to a less negative value, that is, from −1.1 nA to −550 pA, we can inject an effective positive current into the neuron, thus causing depolarization and the firing of APs. Returning I_e to −1.1 nA brings the V_m of the neuron below threshold, inhibiting APs. We can also modulate the neuron's firing rate by changing the I_e with various stimulation patterns (Supplementary Fig. 9).

In addition, the pVC configuration also gains intracellular access by passing a negative electrode current to cause membrane permeabilization. This electrode current is set up indirectly via V_e, which we directly apply, and the pVC configuration also measures this current (Fig. 2c): as we set V_e in the range of −0.6 V to −0.7 V, a negative bias current I_e of approximately −900 pA flows into the electrode. The magnitude of I_e at the onset of intracellular access is similar to that found for the pCC (see Supplementary Fig. 13 for the determination

of these voltage and current values), resulting in a similar small portion (1~10%) of the I_e entering the neuron through R_{jm}. Unlike the pCC with a high input impedance (Z_{eq} in Fig. 2b), the low input impedance of the pVC (Fig. 2c) prevents spontaneous neuron APs during the permeabilization process. Stimulation is therefore used to activate the neuron's ion-channels (Fig. 2f). Negative Na^+ spikes and positive K^+ repolarization currents are observed during these stimulations, as these ion-channel currents I_m cause the change $\Delta I_e = \gamma \times \Delta I_m$ in the electrode current from the bias value. Application of the ion-channel drugs tetrodotoxin (a Na^+ channel blocker) and tetraethylammonium (a K^+ channel blocker) confirm the origins of these signals (Fig. 2g). Determination of the pVC attenuation (γ) is more difficult than for the pCC attenuation (α) because I_m is related to the surface area of the neuronal cell membrane; Na^+ spikes ranging in magnitude from 100 pA to more than 1 nA (for example, in Supplementary Fig. 13a) have been measured. This pVC configuration will be particularly useful for high-throughput ion-channel drug screening applications where planar patch-clamp arrays[14–16] are currently a dominant tool for such applications but are limited to non-neuronal, artificial cell lines.

Network-wide intracellular recording and stimulation

As demonstrated above, an individual pixel of our CNEI performs a stable, controlled intracellular recording of subthreshold PSPs as well as ion-channel currents, similar to the patch-clamp electrode. The key trait that separates the CNEI from the patch-clamp electrode is its scalability: the CNEI parallelizes the high-fidelity intracellular recording with its 4,096 densely populated channels (Fig. 3a,b). We demonstrate this with each pixel configured in pCC mode: with a negative current applied to each pixel electrode ($I_e = -1.1$ nA), we measure intracellular membrane potentials across a network of cultured rat cortical neurons. For example, in the data presented in Fig. 3a (see also Supplementary Videos 1,2), we observe bursts of synchronized firings across the CNEI, and during these bursts, we measure from up to 1,837 pixels in parallel, achieving a coupling rate of about 44 %. The median amplitude of APs during the network bursts in Fig. 3a is approximately 200 μV, but individual amplitudes can be as large as approximately 10 mV.

In another array-wide recording with a duration of 19 min, we performed periodic stimulation (6 s every 1 min) to excite the network and induce more neuronal activity (Fig. 3b and Supplementary Video 3). In the 19-min span, we recorded intracellular signals from 1,728 pixels, with a maximum of 982 pixels intracellularly coupled simultaneously at about 6 min after the start of the current injection. The inset of Fig. 3b (middle) also shows how the number of the simultaneously intracellularly coupled pixels vary with time. The coupling duration of a pixel, defined as the time difference between the first and last recorded intracellular APs, ranged from <10 s to the full duration of the recording, 19 min (limited by the data acquisition rate of 4 GB min^{-1}), with a median of about 8 min (495 s). Figure 3b (middle) presents the histogram showing the distribution of the count of pixels (out of 1,728 intracellularly coupled pixels) over the range of the coupling duration up to 19 min: 569 pixels remain intracellularly coupled over 10 min. The median AP amplitude of each pixel is similar to that of the spontaneous burst of Fig. 3a, but because the typical signal magnitude increases over time (Supplementary Figs. 10 and 11 and Supplementary Discussion 2), the maximum AP amplitude measured at a typical pixel in the experiment shown in Fig. 3b with the increased activity was much higher, with a median value of 2.54 mV.

Network-wide mapping of synaptic connections

With the unique ability to measure subthreshold membrane potentials from many neurons simultaneously, the CNEI in the pCC configuration can locate and characterize synaptic connections and other signal pathways across neuronal networks with a fluency unmatched by patch-clamp electrodes. Figure 3c,d shows example recordings that illustrate this point (extended data for these examples are shown in Supplementary Fig. 14). Network-wide stimulation was first used to find an example of a pair of connected neurons (blue and magenta, Fig. 3c): as we applied a current pulse to every pixel, APs fired in both neurons, but the APs of the presynaptic neuron (blue) also caused closely spaced PSPs in the postsynaptic neuron (magenta), which could summate to reach threshold to fire a new AP about 11.8 ms after the second EPSP (selective stimulation of just a presynaptic neuron is shown in Supplementary Fig. 14b). In Fig. 3d, unstimulated APs in the presynaptic neuron (blue) caused EPSPs in the postsynaptic neuron (magenta) about 260 μm away, whereas closely spaced EPSPs summated to trigger eventual APs. Separately, in Fig. 3d, two neurons (magenta and green) about 80 μm apart with no direct synaptic connection slowly oscillated together, and when these slow oscillations exceeded threshold, the neurons fired temporarily correlated APs often with multiple APs per oscillation (see also Supplementary Fig. 4c). These spatially localized slow oscillations are caused by a local electrochemical field: this was confirmed by the addition of isoguvacine (a γ-aminobutyric acid (GABA) agonist), which increased the frequency of such oscillations (Supplementary Fig. 15 and Supplementary Video 4).

The summation of PSPs into an AP seen in Fig. 3c,d is a characteristic typical of chemical synapses between neurons. A further analysis of measured PSPs reveals another characteristic essential to chemical synapses: the quantization of the PSP amplitudes. For example, consider an excitatory synaptic connection found from a network-wide recording (Fig. 4a and Supplementary Fig. 14d). In this connection between two neurons separated by about 398 μm, each AP in the presynaptic neuron (blue) induces an EPSP in the postsynaptic neuron (magenta) with an average delay of 1.7 ms (this time is consistent with patch recordings of synaptic delays in in vitro networks[42]), with a varying amplitude of the EPSP (Fig. 4a, left). These variable EPSP amplitudes are clearly quantized as multiples of 45 μV (in comparison to the AP amplitude of 5.48 mV) (Fig. 4a, right), which is due to the quantal nature of the chemical synapse. The PSP amplitude quantization has thus far been resolved only with patch-clamp recordings[43,44]. Thus, this study not only confirms that the PSPs we measure are indeed from chemical synaptic connections, but also highlights the high sensitivity of the intracellular recording by the CNEI (these essential characteristics of PSPs have not been apparent in other electrode-based works[27,30,41] that have claimed to measure PSPs). A control experiment (Fig. 4b) shows the reduction of measured EPSP and IPSP activity with the application of synaptic blockers, which further confirms the chemical origin of the synapses.

The key demonstration of the parallelism of PSP-level recording is the explicit mapping of the synaptic connectivity among thousands of neurons across the entire array (Fig. 4c,d). The basic aim of this mapping is to identify and correlate presynaptic APs and resulting PSPs––as we have shown in a few examples, in Figs. 3c,d and 4a––across the array. In particular, we use APs of any given pixel ('origin' pixel) as a trigger for averaging the other 4,095 pixels' signals and identifying the 'target' pixels exhibiting clearly time-correlated PSPs. The detection of these PSPs indicates synaptic connections between the neurons on the origin and target pixels (Supplementary Figs. 16 and 17 and Methods). By applying this process to the array-wide 19-min long intracellular recording data of Fig. 3b, we mapped 304 synaptic connections between 396 neurons (Fig. 4c) among 1,728 neurons that were intracellularly coupled.

Most of these synaptic connections had propagation delays of less than 5 ms with a median of around 2 ms (Fig. 4d, top), suggesting that these connections were monosynaptic, or without intervening neuronal connections. The median pixel distance between pre- and postsynaptic neurons (Fig. 4d, middle) was 228 μm, with a preponderance of shorter synaptic connections: this observation provides a rough measure of the distribution of neurite routing lengths in

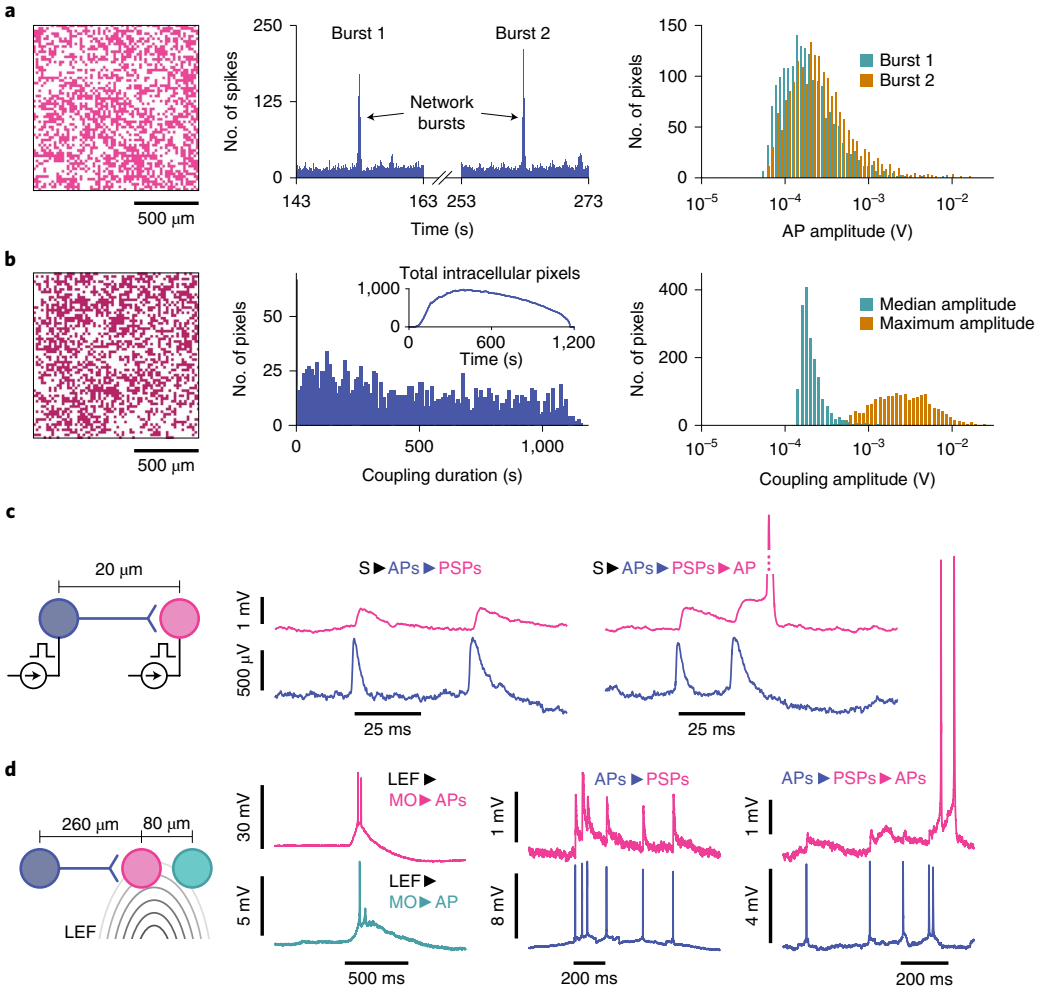

Fig. 3 | Network-wide intracellular measurements of dissociated rat neurons in the pCC configuration. a, Intracellular recordings across the array using $I_e = -1.1$ nA show synchronized firings: large network bursts involving 1,837 pixels (left, burst 1) and 1,882 pixels (burst 2), show correlated spikes (middle, histogram bins of 10 ms) at 153 s and 263 s of the experiment, respectively. The AP spike amplitudes are extracted from both events (right), with an array median of 172 µV and 229 µV, respectively. **b**, Another array-wide intracellular recording, with continual stimulation and a total of 1,728 pixels (left) intracellularly coupled throughout the 19 min recording. The coupling duration (middle, median of 495 s) and AP spike amplitude (right) are characterized. The total number of simultaneously intracellularly coupled pixels as a function of time is plotted in the middle inset, with a maximum of 982 pixels being simultaneously intracellularly coupled at time 396 s. **c**, Array-wide stimulation increases the overall synaptic network activity: stimulated APs of the presynaptic neuron (blue: S▶APs) induce excitatory PSPs in the postsynaptic neuron (magenta, APs▶PSPs). When the PSPs are close enough to summate and exceed threshold, an AP fires (PSPs▶APs). **d**, Spontaneous (non-stimulated) membrane potentials of the middle neuron (magenta) can be related to the left neuron via their synaptic connection (blue) and the local electrochemical field (LEF) that also excites the right neuron (green). APs from the blue neuron induce excitatory PSPs that in turn induce APs. The LEF induces membrane oscillations (MOs); large MOs cause the neurons (magenta and green) to exceed their thresholds to fire APs (MO▶APs).

our array. Moreover, the plot of the propagation delay and distance indicates that the signal propagation speed was about 100 mm s^{-1} (Fig. 4d, bottom), a value consistent with other measured propagation speeds ex vivo[45]. The large variance in the delay–distance correlation is probably due to the random distribution of synaptic cleft propagation delays (as short as 300 µs and up to about 5 ms (refs. [42,46])) and the actual neurite routing deviating from the pre-to-post-synaptic pixel distance.

Discussion

The CNEI's combination of subthreshold sensitivity and parallelism is crucial for accurate and efficient synaptic connectivity mapping. For instance, the analysis of the data in Fig. 3b using AP spike cross-correlations (one of the common methods employed in MEA studies[32,47]; Supplementary Fig. 18) identifies only 63 (21%) out of the 304 connections detected in Fig. 4c. This emphasizes the importance of the CNEI's ability to measure subthreshold PSP signals[45]. Other synaptic mapping methods, notably those that rely on multiple patch clamps[6] or patch clamp in conjunction with Ca^{2+} imaging[1], optogenetic stimulation[2,3] or MEAs[4], are limited by the number of simultaneous patch recordings (less than around 10 versus 4,096 in our CNEI), resulting in prohibitively low throughput for network-wide mapping. Our mapping of the roughly 300 synaptic connections among the over 1,700 intracellularly coupled neurons with only 19 min recording time highlights the experimental throughput.

High-fidelity, simultaneous recording of a large number of connected neurons has long been an important target milestone in electrophysiology. Our CNEI accomplishes this feat for in vitro mammalian neuronal networks. Since in vitro cultures are frequently used for electrophysiological screening of pharmaceutical candidates for neurological disorders, the capability of the CNEI should be readily applicable to, and improve, such phar-

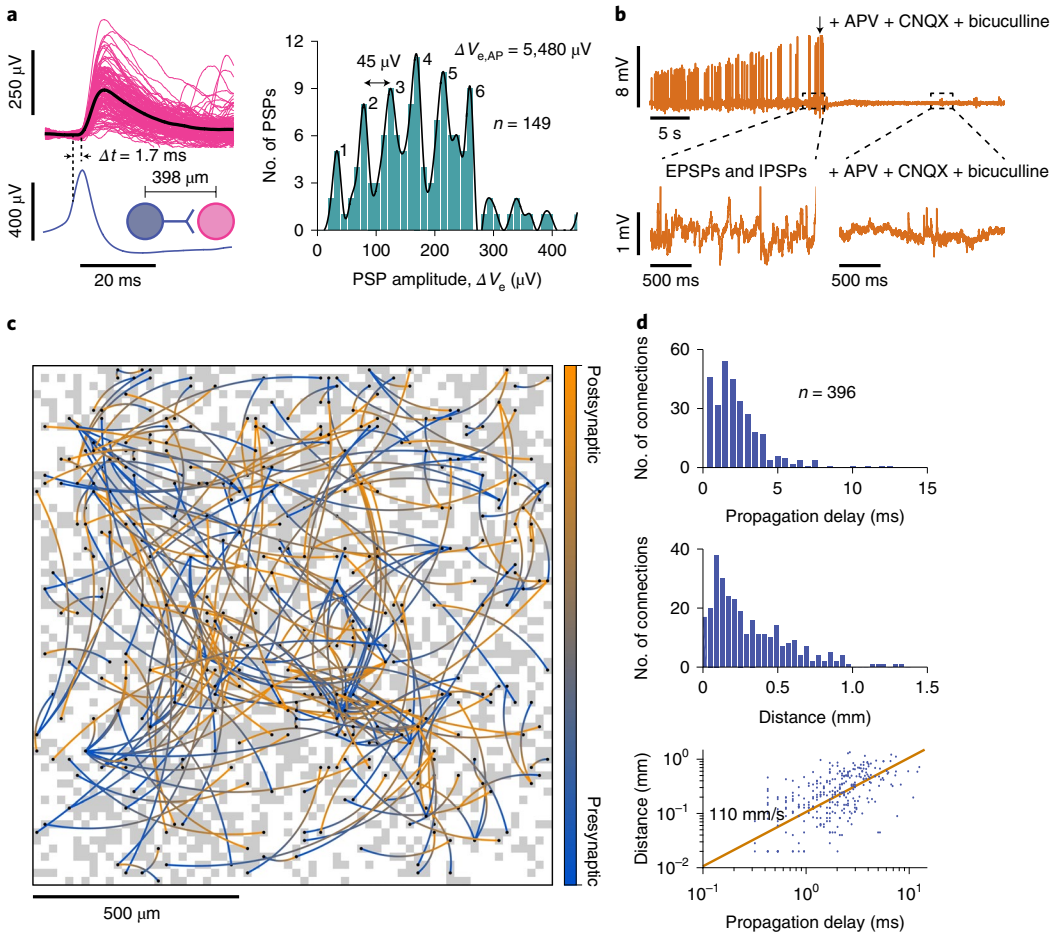

Fig. 4 | Measurement of chemical synapse characteristics and network-wide mapping of synaptic connectivity with the pCC configuration. a, A connection from the presynaptic neuron (blue) to postsynaptic neuron (magenta) displays varying PSP amplitudes (left) with their average shown in black. The synaptic propagation delay, $\Delta t = 1.7$ ms, from the presynaptic neuron AP (average in blue) is estimated. Amplitude histogram of 149 PSPs (right) shows a distinct quantal amplitude of 45 μV (in comparison to an AP amplitude of 5,480 μV). Six quantized amplitudes are clearly observed, the amplitude of around 180 μV being the most frequent. **b**, Addition of 2-amino-5-phosphonovaleric acid (APV, an NMDA (*N*-methyl-D-aspartate) antagonist), cyanquixaline (CNQX, an α-amino-3-hydroxy-5-methyl-4-isoxazole propionic acid (AMPA) antagonist), and bicuculline (a GABA antagonist) to a neuron that exhibits both EPSPs and IPSPs (t_1, upper right), quickly reduces the frequency of PSPs and further AP activity (t_2, lower right). **c**, Connections between presynaptic and postsynaptic neurons are mapped across a neuronal network using spike-triggered averaging. Pixels recording intracellular membrane potentials during the experiment are indicated in grey (the same neuronal network and coupling as in Fig. 3b). A total of 304 synaptic connections between 396 neurons are mapped and indicated with an arced line from the presynaptic (blue) to postsynaptic (orange) neuron's pixels. **d**, Propagation delay (top) and propagation distance (middle) extracted from the network in **c**. Bin sizes are 0.5 ms and 40 μm. Correlation between propagation distance and the propagation delay (bottom), with a best linear speed fit of 110 mm s^{-1}.

maceutical screening applications. Furthermore, its demonstrated compatibility with iPSC-derived neurons (Supplementary Fig. 7c) shows its flexibility with respect to cell type for these applications. The patch clamp has been the traditional method of choice for measuring electrical responses of neurons to chemical inputs, but it has inherently low throughput and is incapable of measuring network dynamics and connections efficiently. By contrast, the CNEI can examine the effects of chemical inputs with much higher throughput and at a network level. Further major improvements in the passive electrode design and the active circuit functions could expand the device capability to ex vivo and in vivo samples, which could have benefits for synaptic connectivity mapping of the brain.

One immediate problem that needs to be addressed to further the capabilities of the device is elongation of the intracellular coupling. Intracellular recording of neurons is known for trading sensitivity with invasiveness, so it is difficult to obtain repeat readings from the same neuron. For instance, patch-clamp recording results in cell death, and similarly, CNEI intracellular recordings could not be repeated in the same neuronal network. Conversely, prolonging the intracellular coupling from the median duration of 8 min––which is already of a similar duration to patch recording––may be more easily achievable by optimizing the leakage compensation. For example, in the pCC configuration, the DC level of the membrane potential could be directly measured and fed back to modify I_e to accurately maintain the DC membrane potential at a suitable value, thus prolonging the duration of intracellular recording. This feedback control would be particularly well suited to semiconductor electronics.

Methods

Electrode fabrication and packaging. We designed the CMOS IC and outsourced its fabrication in 0.18 μm technology to the United Microelectronics Corporation. Subsequently, we post-fabricated the Pt electrodes on the surface Al pads of the CMOS IC in house.

The PtB vertical nanoneedle with pad edge electrodes were fabricated with the following steps (Supplementary Fig. 1a): (1) The original foundry passivation

was removed by dry etching, and a thick metal layer (20 nm Ti, 200 nm Pt) was deposited on the Al pads. (2) A 1-μm thick amorphous Si layer was deposited via chemical vapour deposition. (3) Electron-beam lithography was used to define vertical nanoneedles. (4) Dry etching was performed to etch the amorphous Si layer into ~100-nm diameter vertical nanoneedles. (5) A thin layer of metal (5 nm Ti, 10 nm Pt) was sputtered to make a connection to the pad. A 20-nm thick SiO_2 passivation layer was then deposited via atomic layer deposition. (6) A thin layer of photoresist was spun on the device to cover the nanoneedle base and flat portions surrounding the pad. (7) Wet etching was used to remove the oxide only at the tip of the nanoneedles and at the edge of the pad.

The PtB planar hole electrodes (Supplementary Fig. 1c) were fabricated with the following steps: (1) Photolithography was used to define a 2 μm hole in the foundry passivation layer. (2) The foundry passivation was removed to expose the Al pad by dry etching. (3) A thick layer of metal (20 nm Ti and 200 nm Pt) was deposited to form Pt electrodes.

After the electrode post-fabrication, the CMOS ICs were wire-bonded to chip carriers (Spectrum Semiconductor Materials) with Au wedge bonding. A glass inner ring and outer ring (Friedrich & Dimmock) were glued to the chip and chip carrier, respectively, using polydimethylsiloxane. Polydimethylsiloxane was then poured into the moat between these two glass rings to encapsulate the wire bonds. The well formed by inner ring is where the neurons are cultured after the device is completed with the PtB electrodeposition, as explained next.

PtB electrodeposition. PtB deposition on the Pt electrodes was performed with packaged CMOS ICs, using the same experimental setup as in the electrophysiology experiments (Supplementary Fig. 1f). A solution of 0.5 mM H_2PtCl_6 (Sigma-Aldrich) and 25 mM $NaNO_3$ dissolved in doubly ionized water[26] was poured onto the Pt electrode array. Electrodeposition was then performed by cycling the electrode voltages from 0 V to −1.2 V relative to a Pt reference electrode at a scan rate of 50 mV s^{-1}. Alternating current impedance measurements before and after deposition were performed by applying a 10 mV, 5 kHz sine wave to each electrode in the array sequentially and measuring the resultant current through the Pt reference electrode. To generate uniform impedance across the array, the alternating current impedance was measured periodically throughout the cyclic electrodeposition, and an individual pixel pad's PtB deposition was stopped when its overall impedance reached down to ~300 kΩ (~95 pF). Typically 10~20 cycles were needed to achieve the desired impedance. The devices were re-deposited for ~5 cycles after each neuron experiment to re-gain the low electrode impedance.

Neuron culture and drug application. E18 combined rat neurons from the cortex, hippocampus and ventricular zones were purchased (Brainbits) and cultured according to supplier's protocols. Before each neuron plating, the devices were plasma-treated at 18 W for 5 min, soaked in ethanol for ~5 min while inside a biological hood, rinsed at least five times in sterile DI water and air dried in ambient conditions. The devices were then soaked in 0.1% poly-D-lysine solution dissolved in filtered water (Sigma-Aldrich) at 4 °C overnight, and then washed five times to form a cell-adhesive coating. The neurons were plated on the same day of delivery: neural tissues were dissociated the recommended dissociation medium and adjusted to 10^6 cells ml^{-1}. Each device was seeded with 150,000 cells (150 μl of medium) and replenished with 4 ml of medium 30 min after seeding. Half-medium swaps with NBactive4 (Brainbits) was performed on the second day of plating and every three days thereafter to maintain cell health.

All intracellular rat neuron experiments were performed on 10 to 14 d in vitro (DIV) cultures; the extracellular experiments shown in Supplementary Fig. 6 were performed on 26 to 33 DIV cultures. The iPSC neuron measurements in Supplementary Fig. 7c were performed on 20 DIV iCell GlutaNeurons (FUJIFILM Cellular Dynamics) cultured according to the company's recommended protocols. The electrical measurements were performed in neuron culture medium with a Pt reference electrode. All measurements were performed in the dark to minimize the light sensitivity of the CMOS electronics. The temperature of the CMOS IC was set at 34–37 °C for experiments using the integrated temperature sensors and heater (Supplementary Fig. 3a).

For the drug experiment in Supplementary Fig. 6b, drugs were added to a final concentration of 25 μM APV, 10 μM CNQX and 50 μM bicuculline; eight half-medium exchanges were then performed before the final measurement. For the drug experiment in Supplementary Fig. 6c, CNQX was added to form the concentrations stated; eight half-medium exchanges were then performed before the final measurement. For the drug experiments in Fig. 2g, the electrode voltage was adjusted to gain intracellular access and voltage stimulations of the same amplitude were repeated every 5 s. Either tetrodotoxin dissolved in medium to a final concentration of 33 nM or tetraethylammonium at a final concentration of 1 mM were added. For the drug experiment in Fig. 4b, APV/CNQX/bicuculline were added to a final concentration of (25 μM/10 μM/50 μM). For the drug experiment of Supplementary Fig. 15, isoguvacine was added to a final concentration of 10 μM.

The devices were cleaned with trypsin, soap water and DI water after each neuron culture and were reused after re-deposition of PtB. A typical device could be used for a total of ~100 DIV, showing that the PtB electrodes are capable of passing the required Faradaic current without formation of neurotoxic deposits.

Thirty-nine successful pCC intracellular experiments used 19 CNEI devices (Supplementary Table 1) and 13 rat neuron orders (multiple devices were plated per order). All of the pCC data in the manuscript and Supplementary Information are presented from 13 of these experiments. Fewer pVC intracellular experiments were performed, focusing on single-neuron measurements: the data in the manuscript and Supplementary Information are presented from four of these experiments from an additional three rat neuron orders. Specifically, Fig. 2d and Supplementary Fig. 8 were recorded from the PtB vertical nanoneedle and pad edge electrode device NE1 and neuron culture C1; Figs. 2e, 3c, 4a and Supplementary Fig. 14a,d from device NE2 and C2; Fig. 2f and Supplementary Fig. 13a from PtB vertical nanoneedle (without edge electrode) device N1 and C10; Fig. 2g (left) from N2 and C11; Fig. 2g (right) from N1 and C12; Fig. 3a,d, Supplementary Figs. 7b, 10, 14c, 16, 17 and Supplementary Videos 1 and 2 from NE3 and C3; Figs. 3b, 4c,d, Supplementary Figs. 9d, 18 and Supplementary Video 3 from NE4 and C2; Fig. 4b from NE6 and C5; Supplementary Fig. 3a–c from NE2 and C9; Supplementary Fig. 4 (top) from NE4 and C6; Supplementary Fig. 5 (bottom) from PtB-coated hole electrode device H1 and C7; Supplementary Fig. 5 (middle) from PtB vertical nanoneedles (without edge electrode) device N1 and C8; Supplementary Fig. 7c from NE8 and iPSC-derived neuron culture I1; Supplementary Fig. 9b from NE7 and C4; Supplementary Figs. 9c and 11 from NE3 and C6; Supplementary Fig. 13a,b from NE4 and C10; Supplementary Fig. 13a (bottom) from N1 and C10; Supplementary Fig. 14b from NE5 and C4; Supplementary Fig. 15 and Supplementary Video 4 from NE4 and C3. The extracellular measurements in Supplementary Fig. 6b–d were recorded from two separate neuron orders or cultures using NE6 and NE9.

CMOS IC design and measurement. The architecture and performance of the CMOS IC is a marked improvement from our previous work[8], not only in the array scale and pixel density but, more fundamentally, in the pixel configurations combining the current injector and the voltage amplifier, and noise reduction in the voltage amplifier. The amplifier has a variable-gain bandpass topology, and intracellular experiments were typically performed using a passband gain of ~30 V/V (Supplementary Fig. 3c,d); extracellular experiments were performed with a passband gain of ~300 V/V. The 4,096 amplifier outputs were sampled using 32 integrated 128:1 analogue output multiplexers[8] operating with a 1.20512 MHz clock, resulting in an effective pixel sampling rate of 9.415 kHz. Two National Instruments PXIe-6358 DAQ cards were used for analogue-to-digital conversion.

We characterized the pixel amplifier's voltage gain by applying a sine wave (1 mV amplitude and variable frequency ranging from 0.1 Hz to 100 kHz for Supplementary Fig. 3c; 1 mV amplitude and 100 Hz for Supplementary Fig. 3d) to the amplifier input, with the amplifier output (V_{amp}, with reference to Fig. 2b,c, and Supplementary Figs. 3b and 6a), sampled at 10× the applied frequency. The input referred noise at the V_e node (Supplementary Fig. 3e,f) was determined by measuring the output noise with a DC input signal applied to V_e and dividing it by the measured passband gain (the noise and gain here are measured without solution, as we calculate the input referred noise at the V_e node). The current injector (Supplementary Fig. 3g,h) of each pixel was characterized by an external transimpedance amplifier. We measured and calculated the parasitic routing capacitance, $C_{p,routing}$ (Supplementary Fig. 3b,i,j), by first measuring the gain from $V_{s,1}$ (the positive terminal reference voltage of the operational amplifier; Supplementary Fig. 3b) to V_{amp} with V_e set to a direct-current voltage and then measuring it again with V_e floating. We then used these two gain values and the designed value of C_1 (the amplifier input capacitance, 3.5 pF) and C_2 (the amplifier feedback capacitance, 110 fF) to calculate $C_{p,routing}$. We measured the amplifier's transimpedance gain in the pVC configuration (Supplementary Fig. 3k–m) by applying voltage ramps through C_1 connected to negative terminal of the amplifier to generate current pulses of varying magnitude. The input current noise (Supplementary Fig. 3n) was determined by measuring the output voltage noise with no voltage ramp applied to C_1 and dividing by the measured transimpedance gain (the noise and gain here are measured without solution).

Signal filtering. Data was acquired using LabVIEW software and post-processed using MATLAB. Long (>10 s) trace signals were filtered in the time domain using a single-pole (frequency ranging from 1–100 Hz) high-pass filter. Long traces with stimulations (except the pVC data of Fig. 2f) were first high-pass filtered with the remaining edge of the electrode response zeroed or omitted from the trace (approximately 10 ms to 1 s of data omitted). Short signal traces (<10 s) were not high-pass filtered after acquisition except for Fig. 2g: to eliminate the lower frequency electrode responses (resulting from the electrode's Faradaic resistance, R_s, and R_{jm} in conjunction with the electrode's double layer capacitance) to compare ion-channel currents before and after drug application, we applied a high-pass filter of ~50 Hz. A rolling window average of 3–10 data points was used to lower discretization noise of the analogue-to-digital conversion for slower signals, including Figs. 3c,d and 4b. The short signals of Fig. 2d,f were unfiltered. As mentioned in the main text, all recorded voltages are referred to the V_e node. Scale bars are omitted for synaptic connection data in Supplementary Figs. 16 and 17 due to the variability of the recording attenuation from pixel to pixel and the variation of the coupling amplitude over time.

Spike detection was used to generate Supplementary Videos 1–3, for the peristimulus time histogram (PSTH) in Supplementary Fig. 6b–d, for

characterization in Fig. 3a,b, for the quantal PSP amplitude analysis in Fig. 4a and for the spike-triggered averaging (STA) in Fig. 4c. Data was first high-pass filtered using a frequency of 94 Hz, and then stimulation artifacts were omitted if applicable. Positive spikes larger than five standard deviations were calculated, with each spike time adjusted to the spike's maximum. For the intracellular coupling characterization in Fig. 4b, only pixels that showed clear intracellular signals were included.

PSTH, CNQX titration and STDP stimulation. For the PSTHs in Supplementary Fig. 6b–d, repeated extracellular stimulations were applied to stimulate pixels and spike detection was performed on recording pixels with the time difference between the spike and stimulation binned (histogram bins of 1/9.415 kHz). The extracellular recordings were performed using the transimpedance configuration of the amplifier with V_e adjusted such that $I_{e,DC} = 0$ A. For the titration of Supplementary Fig. 6c, small amounts of high concentration CNQX were added to the culture medium immediately after the PSTH stimulations to form the final concentrations stated, the PSTH stimulation were started at intervals of 10 min. The STDP stimulation of Supplementary Fig. 6d was performed by repeatedly stimulating the stimulation group 1 pixels 10 ms before the stimulation group 2 pixels every 100 ms for 3,000 total stimulations.

Quantal PSP amplitude analysis. For the quantal PSP amplitude analysis in Fig. 4a, spike detection was performed to detect the presynaptic neuron's APs during a 93 s window, totalling 475 spikes. Time windows of 50 ms (10 ms before and 40 ms after the spikes) were then extracted for the postsynaptic neuron's PSPs. Only time windows with a stable baseline for 10 ms before the AP spikes, calculated as $\Delta V_e < 33\,\mu V$, and time windows without APs were used, to enable accurate PSP amplitude measurement: a total of 149 PSP windows met these criteria. Data was smoothed with a rolling window average of 33 data points (3.5 ms) and the difference between maximum to the average of the 10 ms before the AP spikes was used as the PSP amplitude.

STA. For STA, time windows of 75 ms (25 ms before and 50 ms after the spike time) were used to align and average recordings of other pixels. Only pixels with >150 spike times (~1500 pixels) were used for the STA of Fig. 4c and only the largest 500 spikes were used for pixels with >500 spikes. Windows with abnormally large signals (for example, action potentials) in comparison to the other windows were omitted from the averaging to prevent false positives. Averaged signals were sorted by the ratio of the maximum amplitude in the data window to the standard deviation of the outer most 25 ms and then manually inspected. To calculate the propagation delays in Fig. 4d, the averaged data was high-pass filtered using a 100 Hz filter frequency, and the time difference was calculated between the maximum of the presynaptic neuron's signal to the maximum of the postsynaptic neuron's signal. The spike cross-correlation calculation in Supplementary Fig. 18 was performed using a bin width of 1 ms[47].

Reporting Summary. Further information on research design is available in the Nature Research Reporting Summary linked to this article.

Data availability

The authors declare that all data supporting the findings of this study are available within the paper and its Supplementary Information.

Received: 10 April 2018; Accepted: 15 August 2019;
Published online: 23 September 2019

References

1. Sasaki, T., Minamisawa, G., Takahashi, N., Matsuki, N. & Ikegaya, Y. Reverse optical trawling for synaptic connections in situ. *J. Neurophysiol.* **102**, 636–643 (2009).
2. Petreanu, L., Huber, D., Sobczyk, A. & Svoboda, K. Channelrhodopsin-2-assisted circuit mapping of long-range callosal projections. *Nat. Neurosci.* **10**, 663–668 (2007).
3. Shemesh, O. A. et al. Temporally precise single-cell-resolution optogenetics. *Nat. Neurosci.* **20**, 1796–1806 (2017).
4. Jäckel, D. et al. Combination of high-density microelectrode array and patch clamp recordings to enable studies of multisynaptic integration. *Sci. Rep.* **7**, 978 (2017).
5. Spira, M. E. & Hai, A. Multi-electrode array technologies for neuroscience and cardiology. *Nat. Nanotech.* **8**, 83–94 (2013).
6. Perin, R., Berger, T. K. & Markram, H. A synaptic organizing principle for cortical neuronal groups. *Proc. Natl Acad. Sci. USA* **108**, 5419–5424 (2011).
7. Robinson, J. T. et al. Vertical nanowire electrode arrays as a scalable platform for intracellular interfacing to neuronal circuits. *Nat. Nanotech.* **7**, 180–184 (2012).
8. Abbott, J. et al. CMOS nanoelectrode array for all-electrical intracellular electrophysiological imaging. *Nat. Nanotech.* **12**, 460–466 (2017).
9. Eversmann, B. et al. A 128×128 CMOS Biosensor array for extracellular recording of neural activity. *IEEE J. Solid-State Circuits* **38**, 2306–2317 (2003).
10. Berdondini, L. et al. Active pixel sensor array for high spatio-temporal resolution electrophysiological recordings from single cell to large scale neuronal networks. *Lab Chip* **9**, 2644–2651 (2009).
11. Frey, U. et al. Switch-matrix-based high-density microelectrode array in CMOS technology. *IEEE J. Solid-State Circuits* **45**, 467–482 (2010).
12. Tsai, D., Sawyer, D., Bradd, A., Yuste, R. & Shepard, K. L. A very large-scale microelectrode array for cellular-resolution electrophysiology. *Nat. Commun.* **8**, 1802 (2017).
13. Lopez, C. M. et al. A 16,384-electrode 1,024-channel multimodal CMOS MEA for high-throughput intracellular action potential measurements and impedance spectroscopy in drug-screening applications. In *IEEE International Solid-State Circuits Conference* (eds Anderson, J. H. et al.) **61**, 464–466 (IEEE, 2018).
14. Fertig, N., Blick, R. H. & Behrends, J. C. Whole cell patch clamp recording performed on a planar glass chip. *Biophys. J.* **82**, 3056–3062 (2002).
15. Lau, A. Y., Hung, P. J., Wu, A. R. & Lee, L. P. Open-access microfluidic patch-clamp array with raised lateral cell trapping sites. *Lab Chip* **6**, 1510–1515 (2006).
16. Dunlop, J., Bowlby, M., Peri, R., Vasilyev, D. & Arias, R. High-throughput electrophysiology: an emerging paradigm for ion-channel screening and physiology. *Nat. Rev. Drug Discov.* **7**, 358–368 (2008).
17. Hochbaum, D. R. et al. All-optical electrophysiology in mammalian neurons using engineered microbial rhodopsins. *Nat. Methods* **11**, 825–833 (2014).
18. Kim, C. K., Adhikari, A. & Deisseroth, K. Integration of optogenetics with complementary methodologies in systems neuroscience. *Nat. Rev. Neurosci.* **18**, 222–235 (2017).
19. Ikegaya, Y. et al. Synfire chains and cortical songs: temporal modules of cortical activity. *Science* **304**, 559–564 (2004).
20. Stetter, O., Battaglia, D., Soriano, J. & Geisel, T. Model-free reconstruction of excitatory neuronal connectivity from calcium imaging signals. *PLoS Comput. Biol.* **8**, e1002653 (2012).
21. Ahrens, M. B. et al. Brain-wide neuronal dynamics during motor adaptation in zebrafish. *Nature* **485**, 471–477 (2012).
22. Akerboom, J. et al. Optimization of a GCaMP calcium indicator for neural activity imaging. *J. Neurosci.* **32**, 13819–13840 (2012).
23. Gong, Y. et al. High-speed recording of neural spikes in awake mice and flies with a fluorescent voltage sensor. *Science* **350**, 1361–1366 (2015).
24. Woodford, C. R. et al. Improved PeT molecules for optically sensing voltage in neurons. *J. Am. Chem. Soc.* **137**, 1817–1824 (2015).
25. Lou, S. et al. Genetically targeted all-optical electrophysiology with a transgenic cre-dependent optopatch mouse. *J. Neurosci.* **36**, 11059–11073 (2016).
26. Li, L.-L. et al. Morphological control of platinum nanostructures for highly efficient dye-sensitized solar cells. *J. Mater. Chem.* **22**, 6267 (2012).
27. Dipalo, M. et al. Intracellular and extracellular recording of spontaneous action potentials in mammalian neurons and cardiac cells with 3D plasmonic nanoelectrodes. *Nano Lett.* **17**, 3932–3939 (2017).
28. Lin, Z. C., Xie, C., Osakada, Y., Cui, Y. & Cui, B. Iridium oxide nanotube electrodes for sensitive and prolonged intracellular measurement of action potentials. *Nat. Commun.* **5**, 3206 (2014).
29. Hai, A., Shappir, J. & Spira, M. E. In-cell recordings by extracellular microelectrodes. *Nat. Methods* **7**, 200–202 (2010).
30. Liu, R. et al. High density individually addressable nanowire arrays record intracellular activity from primary rodent and human stem cell derived neurons. *Nano Lett.* **17**, 2757–2764 (2017).
31. Fromherz, P. Self-gating of ion channels in cell adhesion. *Phys. Rev. Lett.* **78**, 4131–4134 (1997).
32. Obien, M. E. J., Deligkaris, K., Bullmann, T., Bakkum, D. J. & Frey, U. Revealing neuronal function through microelectrode array recordings. *Front. Neurosci.* **9**, 423 (2015).
33. Massobrio, P., Tessadori, J., Chiappalone, M. & Ghirardi, M. In vitro studies of neuronal networks and synaptic plasticity in invertebrates and in mammals using multielectrode arrays. *Neural Plast.* **2015**, 1–18 (2015).
34. Froemke, R. C., Debanne, D. & Bi, G.-Q. Temporal modulation of spike-timing-dependent plasticity. *Front. Syn. Neurosci.* **2**, 19 (2010).
35. Hai, A. & Spira, M. E. On-chip electroporation, membrane repair dynamics and transient in-cell recordings by arrays of gold mushroom-shaped microelectrodes. *Lab Chip* **12**, 2865–2873 (2012).
36. Xie, C., Lin, Z., Hanson, L., Cui, Y. & Cui, B. Intracellular recording of action potentials by nanopillar electroporation. *Nat. Nanotech.* **7**, 185–190 (2012).
37. Duan, X. et al. Intracellular recordings of action potentials by an extracellular nanoscale field-effect transistor. *Nat. Nanotechnol.* **7**, 174–179 (2012).
38. Lee, K.-Y. et al. Vertical nanowire probes for intracellular signaling of living cells. *Nanoscale Res. Lett.* **9**, 56 (2014).
39. Tian, B. et al. Three-dimensional, flexible nanoscale field-effect transistors as localized bioprobes. *Science* **329**, 830–834 (2010).
40. Hai, A., Shappir, J. & Spira, M. E. Long-term, multisite, parallel, in-cell recording and stimulation by an array of extracellular microelectrodes. *J. Neurophysiol.* **104**, 559–568 (2010).

41. Shmoel, N. et al. Multisite electrophysiological recordings by self-assembled loose-patch-like junctions between cultured hippocampal neurons and mushroom-shaped microelectrodes. *Sci. Rep.* **6**, 27110 (2016).
42. Fitzsimonds, R. M., Song, H. J. & Poo, M. M. Propagation of activity-dependent synaptic depression in simple neural networks. *Nature* **388**, 439–448 (1997).
43. Kullmann, D. M. & Nicoll, R. A. Long-term potentiation is associated with increases in quantal content and quantal amplitude. *Nature* **357**, 240–244 (1992).
44. Hardingham, N. R. et al. Quantal analysis reveals a functional correlation between presynaptic and postsynaptic efficacy in excitatory connections from rat neocortex. *J. Neurosci.* **30**, 1441–1451 (2010).
45. Shein-Idelson, M., Pammer, L., Hemberger, M. & Laurent, G. Large-scale mapping of cortical synaptic projections with extracellular electrode arrays. *Nat. Methods* **14**, 882–890 (2017).
46. Sabatini, B. L. & Regehr, W. G. Timing of neurotransmission at fast synapses in the mammalian brain. *Nature* **384**, 170–172 (1996).
47. Barthó, P. et al. Characterization of neocortical principal cells and interneurons by network interactions and extracellular features. *J. Neurophysiol.* **92**, 600–608 (2004).

Acknowledgements

Post-fabrication and characterization were performed, in part, at the Center for Nanoscale Systems at Harvard University. The authors are grateful for the support of this research by Samsung Advanced Institute of Technology, Samsung Electronics (A37734 to H.P. and D.H.), Catalyst Foundation (J.A., H.P. and D.H.), the Army Research Office (W911NF-15-1-0565 to D.H.), the Army Research Office (W911NF-17-1-0425 to D.H.), the National Science Foundation Graduate Research Fellowship Program (DGE1745303 to K.K.), the National Institutes of Health (1-U01-MH105960-01 to H.P.), the Gordon and Betty Moore Foundation (to H.P.), and the US Army Research Laboratory and the US Army Research Office (W911NF1510548 to H.P.).

Author contributions

H.P., D.H., J.A., T.Y. and K.K. conceived and designed the experiments. J.A. and L.Q. designed the CMOS IC, J.A., Y.K. and W.W. designed the interface electronics and T.Y., S.B. and K.K. performed post-fabrication and device packaging. J.A., T.Y., K.K. and R.S.G. performed the experiments and J.A., T.Y., K.K., H.P. and D.H. analysed the data. H.P. and D.H. supervised the project. J.A., T.Y., K.K., D.H. and H.P. wrote the manuscript, and all authors read and discussed it.

Competing interests

The authors declare no competing interests.

Additional information

Supplementary information is available for this paper at https://doi.org/10.1038/s41551-019-0455-7.

Reprints and permissions information is available at www.nature.com/reprints.

Correspondence and requests for materials should be addressed to H.P. or D.H.

Publisher's note Springer Nature remains neutral with regard to jurisdictional claims in published maps and institutional affiliations.

© The Author(s), under exclusive licence to Springer Nature Limited 2019

nature research

Corresponding author(s): Hongkun Park & Donhee Ham

Last updated by author(s): Aug 9, 2019

Reporting Summary

Nature Research wishes to improve the reproducibility of the work that we publish. This form provides structure for consistency and transparency in reporting. For further information on Nature Research policies, see Authors & Referees and the Editorial Policy Checklist.

Statistics

For all statistical analyses, confirm that the following items are present in the figure legend, table legend, main text, or Methods section.

n/a	Confirmed	
☒	☐	The exact sample size (*n*) for each experimental group/condition, given as a discrete number and unit of measurement
☐	☒	A statement on whether measurements were taken from distinct samples or whether the same sample was measured repeatedly
☒	☐	The statistical test(s) used AND whether they are one- or two-sided *Only common tests should be described solely by name; describe more complex techniques in the Methods section.*
☒	☐	A description of all covariates tested
☒	☐	A description of any assumptions or corrections, such as tests of normality and adjustment for multiple comparisons
☐	☒	A full description of the statistical parameters including central tendency (e.g. means) or other basic estimates (e.g. regression coefficient) AND variation (e.g. standard deviation) or associated estimates of uncertainty (e.g. confidence intervals)
☒	☐	For null hypothesis testing, the test statistic (e.g. *F*, *t*, *r*) with confidence intervals, effect sizes, degrees of freedom and *P* value noted *Give P values as exact values whenever suitable.*
☒	☐	For Bayesian analysis, information on the choice of priors and Markov chain Monte Carlo settings
☒	☐	For hierarchical and complex designs, identification of the appropriate level for tests and full reporting of outcomes
☒	☐	Estimates of effect sizes (e.g. Cohen's *d*, Pearson's *r*), indicating how they were calculated

Our web collection on statistics for biologists contains articles on many of the points above.

Software and code

Policy information about availability of computer code

Data collection	Labview software was used for programming the device and for data acquisition.
Data analysis	MATLAB scripts were used for analysis of the acquired data. The scripts digitally filtered the data, performed spike detection, and spike-triggered-averaging. The specifics of these analyses are detailed in Methods.

For manuscripts utilizing custom algorithms or software that are central to the research but not yet described in published literature, software must be made available to editors/reviewers. We strongly encourage code deposition in a community repository (e.g. GitHub). See the Nature Research guidelines for submitting code & software for further information.

Data

Policy information about availability of data

All manuscripts must include a data availability statement. This statement should provide the following information, where applicable:

- Accession codes, unique identifiers, or web links for publicly available datasets
- A list of figures that have associated raw data
- A description of any restrictions on data availability

The authors declare that all data supporting the findings of this study are available within the paper and its Supplementary Information.

Field-specific reporting

Please select the one below that is the best fit for your research. If you are not sure, read the appropriate sections before making your selection.

☒ Life sciences ☐ Behavioural & social sciences ☐ Ecological, evolutionary & environmental sciences

Life sciences study design

All studies must disclose on these points even when the disclosure is negative.

Sample size	We include data from 43 experiments using 19 CNEI devices and 16 neuron orders (multiple devices were plated per order). All of the data in the manuscript and Supplementary Information are presented from 17 of these experiments, and further statistics from all of these experiments are included in the Supplementary Information.
Data exclusions	No data were excluded from the analyses.
Replication	Experiments were performed multiple times with different devices and cultures. Intracellular recordings from hundreds to thousands of neurons were confirmed throughout the majority of these experiments; the extant of coupling depended on device and culture conditions.
Randomization	Experimental groups were not relevant to our study, as we do not need to compare to a control to determine intracellular recordings.
Blinding	No groups were used, therefore blinding was not necessary.

Reporting for specific materials, systems and methods

We require information from authors about some types of materials, experimental systems and methods used in many studies. Here, indicate whether each material, system or method listed is relevant to your study. If you are not sure if a list item applies to your research, read the appropriate section before selecting a response.

Materials & experimental systems

n/a	Involved in the study
☒	☐ Antibodies
☒	☐ Eukaryotic cell lines
☒	☐ Palaeontology
☒	☐ Animals and other organisms
☒	☐ Human research participants
☒	☐ Clinical data

Methods

n/a	Involved in the study
☒	☐ ChIP-seq
☒	☐ Flow cytometry
☒	☐ MRI-based neuroimaging